Amortized Inference for Heterogeneous Reconstruction in Cryo-EM

Anonymous Author(s)
Affiliation
Address
email

Abstract

Cryo-electron microscopy (cryo-EM) is an imaging modality that provides unique insights into the dynamics of proteins and other building blocks of life. The algorithmic challenge of jointly estimating the poses, 3D structure, and conformational heterogeneity of a biomolecule from millions of noisy and randomly oriented 2D projections in a computationally efficient manner, however, remains unsolved. Our method, cryoFIRE, performs *ab initio* heterogeneous reconstruction with unknown poses in an amortized framework, thereby avoiding the computationally expensive step of pose search while enabling the analysis of conformational heterogeneity. Poses and conformation are jointly estimated by an encoder while a physics-based decoder aggregates the images into an implicit neural representation of the conformational space. We show that our method can provide one order of magnitude speedup on datasets containing millions of images, without any loss of accuracy. We validate that the joint estimation of poses and conformations can be amortized over the size of the dataset. For the first time, we prove that an amortized method can extract interpretable dynamic information from experimental datasets.

1 Introduction

Proteins and other biological macromolecules in the cell function through a finely-tuned choreography of transitions between metastable conformational states. Analyzing the structural heterogeneity of a biomolecule is therefore critical for applications such as drug design and, more generally, for understanding these essential building blocks of life. In a single particle cryo-electron microscopy (cryo-EM) experiment, a set of biomolecules whose structures sample some thermodynamic distribution are flash-frozen in a thin layer of vitreous ice and imaged with a transmission electron microscope (Fig. 1 (a)). A cryo-EM experiment outputs a large set of unlabeled images, each containing a unique projected molecule that adopts an unknown conformation and is viewed from an unknown orientation (*pose*) $\phi_i = (R_i, \mathbf{t}_i) \in SO(3) \times \mathbb{R}^2$ (Fig. 1 (b)). While *homogeneous* reconstruction methods focus on estimating the average 3D structure (the *consensus* volume) of the studied molecule from the collected images, *heterogeneous* methods take into account structural variability and introduce a variable z_i (the *conformational state*) that characterizes the electron scattering potential (the *volume*) $\mathcal{V}(., z_i) : \mathbb{R}^3 \to \mathbb{R}$ associated with observation i [5]. Given the image formation model (detailed in Section 3.1), heterogeneous reconstruction can be seen as an inverse problem where $\mathcal{V}$, z_i and ϕ_i must be inferred from the images Y_i. A graphical formulation of the problem is given in Fig. 1 (c).

Spurred by recent advances in data collection capabilities, the number of images collected per cryo-EM experiments has been steadily increasing, now reaching millions to tens of millions [2, 17]. Established methods break down 3D reconstruction into two alternating iterative refinement steps: 1) the *latent* pose ϕ_i and conformational states z_i are first estimated from the images and the current estimate of $\mathcal{V}$, and 2) the estimation of $\mathcal{V}$ is then updated using the current estimates of the latent

Submitted to 36th Conference on Neural Information Processing Systems (NeurIPS 2022). Do not distribute.

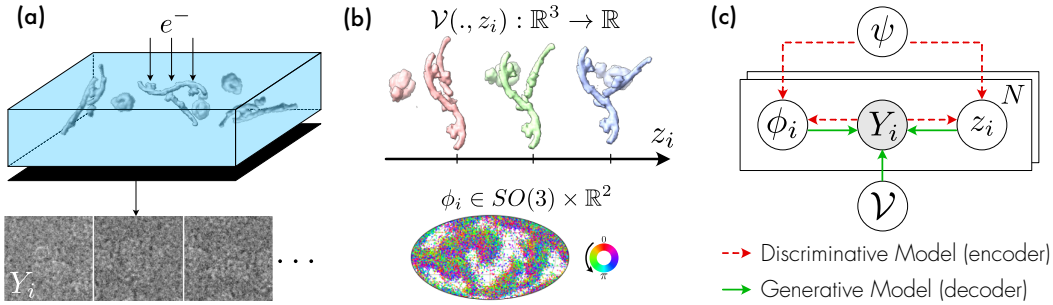

Figure 1: (a) Illustration of a cryo-EM experiment. Molecules are frozen in a random orientation ϕ_i and in a random conformation z_i. Their electron scattering potential $\mathcal{V}(., z_i)$ interacts with an electron beam resulting in noisy projected images Y_i on the detector. (b) (Top) Example representation of scattering potentials in the conformational space $\mathcal{V}$ visualized as an isosurface. (Bottom) Poses are characterized by a rotation in $SO(3)$ and a translation in $\mathbb{R}^2$ (not shown). (c) Graphical model for our method. The encoder, parameterized by ψ, is a discriminative model that predicts ϕ_i and z_i from Y_i while the decoder is a generative model that outputs a noise-free estimation of the image.

variables. The primary computational bottleneck of this approach is pose estimation, which is done by rendering images from view points distributed on the the 5-dimensional space $SO(3) \times \mathbb{R}^2$. Although previous methods came up with accelerated branch-and-bound [13] strategies, state-of-the-art methods for pose search raise two problems: (1) solving this problem for a single image is time consuming, especially when the images are rendered using a neural model [35] and (2) the pose needs to be solved independently for each image in the dataset and does not use the fact that similar images are likely associated with the similar variables. Furthermore, most heterogeneous reconstruction algorithms limit their applicability by relying on an upstream homogeneous reconstruction, treating poses as known to simplify the optimization problem for z_i or due to the sheer computational cost of pose search.

In this work, we present an amortized inference approach to heterogeneous cryo-EM reconstruction, addressing both the increasing size of datasets and the opportunity to learn complex conformational spaces of dynamic proteins. Our method performs *ab initio* reconstruction, meaning it does not need an upstream homogeneous reconstruction. Previous methods showed that the estimation of z_i could be amortized in heterogeneous reconstruction [33, 35, 4, 36] and that the estimation of ϕ_i could be amortized in homogeneous reconstruction [18, 14] but no jointly amortized inference technique was proven to work on experimental datasets. By leveraging a tailored loss function and using a specialized autoencoder-like architecture, cryoFIRE (Fast heterogeneous ab Initio Reconstruction for cryo-EM) jointly amortizes the estimation of poses and conformations over the size of the dataset. Our contributions include:

- an autoencoder-based architecture that process images 10 times faster than existing methods and enables amortization of the runtime over the size of the dataset,
- a demonstration that our model accurately learns the structure of a low-dimensional manifold in the conformational space on benchmark synthetic datasets with both discrete and continuous heterogeneity, and
- the first instance of amortized inference for *ab initio* heterogeneous reconstruction of experimental cryo-EM datasets.

2 Related Work

Heterogeneous reconstruction methods must jointly infer the conformational space $\mathcal{V}$ and the latent variables (the poses ϕ and the conformational states z_i). All existing methods make this problem tractable using an iterative strategy that alternates between the estimation of $\mathcal{V}$ and the estimation of the latent variables. They can all be differentiated depending on how latent variables are estimated [5].

Expectation-Maximization over Conformations With an Expectation-Maximization (EM) algorithm, posterior distributions over the conformational states are computed (or approximated) for each image at expectation step. In cryo-EM, this method was first popularized by RELION with 3D Classification [27] which implemented a discrete class indicator $z_i \in \{1, \ldots, K\}$, where K is the number of classes defined by the user. More recently, a continuous reconstruction method called *multi-body refinement* was made available in RELION [16]. In this approach, a homogeneous reconstruction is segmented by the user into a set of rigid bodies, where each rigid body is free to move relative to the others. The relative pose (orientation and translation) of each body is subsequently estimated through EM for each particle, and further reduced through Principal Component Analysis (PCA). Various methods have been developed to estimate the conformational space as a linear deformation around a known reference. HEMNMA [8] uses the normal modes, or eigenvolumes, of the reference to model its deformation and proceeds through a projection-matching-based elastic alignment of each single-particle image with the reference structure to yield a reduced representation of the variability in the dataset. 3DVA [21] relaxes the dependence on known normal modes and instead implements a variant of the EM algorithm for Probabilistic PCA which iteratively updates the eigenvolumes and the projection of the particles on them, until convergence, following [30]. Other approaches explicitly estimate the deformation field mapping the reference structure to the best-fit structure for each image. In Herreros et al. [7], the deformation field is defined as a linear expansion over Zernike polynomials, with z_i as their coefficients. In 3DFlex [20], the deformation field is generated from z_i through a neural flow generator, alleviating the linear constraint. Formally, each z_i can be seen as a point estimate that maximizes the posterior distribution over conformational states. An in-depth review of EM-based reconstruction method can be found in [29].

Amortization over Conformations Instead of optimizing each variable independently, amortized inference learns a function q_ψ, parameterized by ψ, that maps images Y_i to probability (posterior) distributions over the space of latent variables [10]. CryoDRGN [33] introduced amortized variational inference to estimate the conformational state z_i in the setting where poses are known. In cryoDRGN [33], distributions over the conformational states are predicted by the encoder of a Variational Autoencoder (VAE) [10, 11] and the conformational space is parameterized with an implicit neural representation. E2GMM [4] and cryoFold [36] both reconstruct a deformable atomic representation of the molecule and train an encoder to associate each image with a low-dimensional z_i that characterizes the deformation. These two methods require the initialization of the backbone structure of the molecule. Although these methods can be used to analyze the structural heterogeneity in a dataset, they assume the poses to be given by another reconstruction method. In cryoDRGN-BNB [34] and cryoDRGN2 [35] the poses are not given anymore but instead are estimated using an exhaustive search strategy. The estimation of the poses therefore does not amortize over the size of the dataset and, in spite of a branch-and-bound approach [13], the 5D pose search remains the most computationally expensive step in the pipeline.

Amortization over Poses In the context of homogeneous reconstruction, previous methods used amortized inference to predict the poses. In cryoVAEGAN [15], Miolane *et al.* showed that the in-plane rotation could be disentangled from the contrast transfer function (CTF) parameters in the latent space of an encoder. CryoPoseNet [18] first demonstrated the possibility of using an autoencoder architecture with synthetic datasets. CryoAI [14] later introduced the *symmetrized loss* to help the model avoid local minima and showed that homogeneous reconstruction could be done on experimental datasets. All of these methods, however, reconstruct a 3D *consensus* volume and do not address the question of conformational heterogeneity.

Joint Amortization Rosenbaum *et al.*. [24] were the first to demonstrate heterogeneous reconstruction from unknown poses in a jointly amortized framework on synthetic data: both z_i and ϕ are estimated with a variational encoder and predicted conformations are used to deform an atomic model, while predicted poses are used to compute projections analytically. The method was only proven to work on simulated datasets. To the best of our knowledge, no amortized inference technique was proven to work with experimental datasets in a heterogeneous reconstruction setting with unknown poses.

Our approach (cryoFIRE) uses a conditioned neural network to implicitly represent the conformational space $\mathcal{V}$. An encoder amortizes the inference of both z_i and ϕ_i over the size of the dataset and a differentiable rendering pipeline generates noise-free images. In contrast to previous techniques that

jointly amortize the estimation of ϕ_i and z_i, cryoFIRE can perform heterogeneous reconstruction on experimental datasets.

3 Methods

3.1 Image Formation Model

In single particle cryo-EM, probing electrons interact with the electrostatic potential created by the molecules embedded in a thin layer of vitreous ice (Figure 1 (a)). During reconstruction, we assume that this potential can be broken down into spatially bounded independent potentials (*volumes*) created by individual molecules. Each volume V_i can be seen as a mapping from $\mathbb{R}^3$ to $\mathbb{R}$ and is indexed by $i \in \{1, \ldots, N\}$. We assume that the volumes $\{V_i\}_{i=1,\ldots,N}$ are drawn independently from a probability distribution $\mathbb{P}_V$ supported on a low-dimensional manifold (the *conformational space*) in the space $\mathcal{F}(\mathbb{R}^3, \mathbb{R})$ of all possible 3D potentials. More specifically, we assume there exist $d \in \mathbb{N}$ and $\mathcal{V} : \mathbb{R}^3 \times \mathbb{R}^d \to \mathbb{R}$ such that $\mathbb{P}_V$ is supported on the conformational space $\{\mathcal{V}(., z), z \in \mathbb{R}^d\}$.

In the sample, each molecule is in an unknown orientation $R_i \in SO(3) \subset \mathbb{R}^{3\times 3}$ in the frame of the observer. The probing electron beam interacts with the electrostatic potential and its projections,

$$Q_i : (x, y) \mapsto \int_t \mathcal{V}\left(R_i \cdot [x, y, t]^T, z_i\right) dt \tag{1}$$

are considered mappings from $\mathbb{R}^2$ to $\mathbb{R}$. The interaction between the beam and the lens is modeled by the Point Spread Function (PSF) P_i. Imperfect centering of the molecule in the image is characterized by small translations $\mathbf{t}_i \in \mathbb{R}^2$. Finally, taking into account signal arising from the vitreous ice into which the molecules are embedded as well as the non-idealities of the lens and the detector, each image Y_i is generally modeled as

$$Y_i = T_{\mathbf{t}_i} * P_i * Q_i + \eta_i \tag{2}$$

where $*$ is the convolution operator, $T_{\mathbf{t}}$ the $\mathbf{t}$-translation kernel and η_i white Gaussian noise on $\mathbb{R}^2$ [32, 26].

The Fourier-Slice Theorem [3] (FST) avoids the computation of integrals and convolutions in Eq. (2) and is also satisfied with the Hartley transform:

$$\mathcal{H}_{2\text{D}}\left[Q_i\right] = \mathcal{S}_i\left[\mathcal{H}_{3\text{D}}\left[\mathcal{V}(., z_i)\right]\right], \tag{3}$$

where $\mathcal{H}_{2\text{D}}$ and $\mathcal{H}_{3\text{D}}$ are the 2D and 3D Hartley transform operators [6]. The "slice" operator $\mathcal{S}_i$ is defined such that for any $\hat{V} : \mathbb{R}^3 \to \mathbb{R}$,

$$\mathcal{S}_i[\hat{V}] : (k_x, k_y) \mapsto \hat{V}\left(R_i \cdot [k_x, k_y, 0]^T\right). \tag{4}$$

Finally, if $\hat{Y}_i = \mathcal{H}_{2\text{D}}[Y_i]$ and $\hat{\mathcal{V}}(., z_i) = \mathcal{H}_{3\text{D}}\left[\mathcal{V}(., z_i)\right]$, the image formation model in Hartley space can be expressed as

$$\hat{Y}_i = \hat{T}_{\mathbf{t}_i} \odot C_i \odot \mathcal{S}_i[\hat{\mathcal{V}}(., z_i)] + \hat{\eta}_i, \tag{5}$$

where $\odot$ indicates element-wise multiplication, $C_i = \mathcal{H}_{2\text{D}}\left[P_i\right]$ is the Contrast Transfer Function (CTF), $\hat{T}_{\mathbf{t}}$ the $\mathbf{t}$-translation operator or phase-shift in Fourier space and $\hat{\eta}_i$ represents complex white Gaussian noise on $\mathbb{R}^2$.

3.2 Overview of cryoFIRE

Fig. 2 summarizes the architecture of cryoFIRE. Images Y_i are fed into an encoder, parameterized by ψ, that predicts a pose $\phi = (R_i, \mathbf{t}_i)$ and a conformational state z_i. R_i is used to rotate a grid of D^2 3D-coordinates in Hartley space. These coordinates are concatenated with the conformational state before being fed into a neural representation of the function $\hat{\mathcal{V}}_\theta$ (in Hartley space), parameterized by θ. $\hat{\mathcal{V}}_\theta$ is a mapping from $\mathbb{R}^{3+d}$ to $\mathbb{R}$ and can be seen as a parametric representation of the conformational space in Hartley domain (a manifold of dimension d). Queried for all $\mathbf{k}$ in the grid, the neural representation outputs a set of real values corresponding to a discrete sampling of the slice defined in Eq. (4). Based on the estimated translation $\mathbf{t}_i$ and given CTF parameters C_i, the rest of the image formation model described in Eq. (5) is simulated to obtain $\hat{X}_i$, a noise-free estimation of $\hat{Y}_i$.

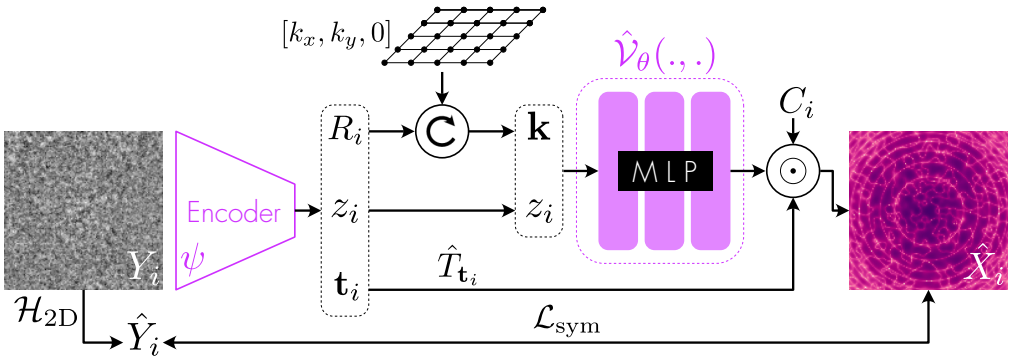

Figure 2: Autoencoder-like architecture. An encoder predicts the latent variable z_i (conformational state), R_i (rotation) and $\mathbf{t}_i$ (translation) for each image. These variables are used by a physics-based decoder that reproduces the image formation model (in Hartley space) and contains a neural representation $\hat{\mathcal{V}}_\theta$ of the conformational space. Reconstructed and measured images are compared with the symmetrized loss.

The whole forward model is refered to as $\Gamma_{\psi,\theta}$, such that $\hat{X}_i = \Gamma_{\psi,\theta}(Y_i)$. Pairs of measured and reconstructed images are compared using the symmetrized loss (see Section 3.5) and gradients are backpropagated throughout the differentiable model in order to optimize both the encoder and the neural representation.

3.3 Discriminative Model

In cryoFIRE, an encoder acts as a discriminative model by mapping images to estimates of ϕ_i and z_i. The encoder is structured sequentially with the following components:

1. A Convolutional Neural Network (CNN) containing 7 convolutional layers extracts high-level visual features from images and divides the width and height of images by 32. The architecture of the CNN is inspired from the first layers of VGG16 [28], known to perform well on visual tasks.
2. A *shared* Multi-Layer Perceptron (MLP) with 2 hidden layers that outputs a feature y_i of dimension 256.
3. A *conformation* MLP that maps y_i to z_i.
4. *Rotation* and *translation* MLPs that map the concatenation of y_i and z_i respectively to R_i and $\mathbf{t}_i$. The pose prediction is conditioned on z_i since rotations and translations are only defined for a given conformation of the molecule and z_i contains, with a small number of dimensions, all the required information to determine the conformational state. The rotation is represented in the 6-dimensional space $\mathcal{S}^2 \times \mathcal{S}^2$ [37].

We experimented with both variational (predicting an approximate posterior distribution over latent variables) and non-variational (predicting a point estimate) approaches and did not observe any significant performance difference (although the variational approach is more computationally expensive). Full details about the architecture of the encoder are given in Supplement A.

3.4 Generative Model

The generative model is a simulation of the image formation model in Hartley space, in order to make use of the FST (Section 3.1). The forward pass is differentiable with respect to z_i, R_i and $\mathbf{t}_i$. For each i, a grid of D^2 coordinates on the x-y plane in Hartley space are rotated by R_i (mapped from $\mathcal{S}^2 \times \mathcal{S}^2$ to $\mathbb{R}^{3\times3}$ using Gram–Schmidt orthogonalization) *via* a matrix multiplication. Rotated points $\mathbf{k}$ are positionally encoded with a bank of $D/2$ random frequencies [31] and independently concatenated with the conformational state z_i before being fed into an MLP mapping $\mathbb{R}^{3+d}$ to $\mathbb{R}$. This neural network is an implicit representation of the function $\hat{\mathcal{V}}$, where $\hat{\mathcal{V}}(.,z) = \mathcal{H}_{3D}\left[\mathcal{V}(.,z)\right]$. Additional implementation details about the neural network are given in Supplement B.

The CTF is defined by the *defoci* parameters and the *astigmatism angle* (provided by the simulator or by an external software like CTFFIND [23] for experimental datasets). It is then applied to the slice of size D^2 outputted by the neural representation. Finally, the slice is element-wise multiplied by $\hat{T}_{\mathbf{t}_i}$, the Hartley transform of the $\mathbf{t}_i$-translation kernel.

3.5 Training Procedure

In the setting where poses are unknown, one cannot distinguish, given a set of 2D projections, two molecules with different handedness. This is called the "handedness ambiguity" [25]. Ref. [14] showed that this leads amortized inference techniques to get stuck in local minima where the predicted molecule contains spurious planar symmetries. A solution suggested to alleviate this problem is to use the *symmetrized loss*

$$\mathcal{L}_{\text{sym}} = \sum_{i \in \mathcal{B}} \min \left\{ \|\hat{Y}_i - \Gamma_{\psi,\theta}(Y_i)\|_2^2, \|\mathcal{R}_\pi[\hat{Y}_i] - \Gamma_{\psi,\theta}\left(\mathcal{R}_\pi\left[Y_i\right]\right)\|_2^2 \right\}, \tag{6}$$

where $\mathcal{B}$ is a batch of indices and $\mathcal{R}_\pi$ applies an in-plane rotation of π on images. In order to enable the model to converge to a consensus volume, we disable the optimization of the conformation MLP at the start of the training. During this "pose-only phase", z_i are randomly sampled from a normalized Gaussian distribution.

4 Results

We evaluate cryoFIRE for *ab initio* heterogeneous reconstruction and compare it with the state-of-the-art method cryoDRGN2 [35]. We first validate that using an encoder to predict poses, instead of performing an exhaustive pose search, enables us to reduce the runtime of heterogeneous reconstruction on a synthetic dataset. We show that the encoder is able to accurately predict ϕ_i and z_i for images it has never processed during training, thereby validating the ability of an encoder-like architecture to amortize the runtime over the size of the dataset. Secondly, we show that cryoFIRE enables the detection of discrete heterogeneity in a dataset, by clustering images in the z_i-space. Finally, we show that our method can perform heterogeneous reconstruction of real data, a first for a method that jointly amortizes the estimation of poses and conformations.

4.1 Runtime Improvement and Amortization

Experimental Setup We prepare three synthetic datasets of varying sizes – *small* (50k images), *medium* (500k images) and *large* (5M images) (Supplement C). Images are generated using a simulation of the image formation model on ground truth volumes of the 80S ribosome. Each dataset contains a mix of projections with 90% sampled from the *major* volume and the rest from the *minor* volume. CTFs are drawn randomly with a log-normal distribution over the defocus range. We add Gaussian noise with standard deviation $\sigma = 1$ to the normalized projections. With cryoFIRE, we fix $d = 8$ and activate the conformation MLP after the model has seen 1.5M images. We compare our method with cryoDRGN2 [35] with default parameters. Images are masked with a circle of radius 32 pixels for pose search. Pose search is done every 5 epochs for the small datasets and every epoch for the medium and large datasets. We train the models on a single NVIDIA A100 SXM4 40GB GPU. Images of size $D = 128$ are fed by batches of maximum sizes (128 for cryoFIRE, 32 for cryoDRGN2) and loaded on the fly using multi-threading on 16 CPUs. The model is optimized with the ADAM optimizer [9] and a learning rate of 10^{-4}. Convergence is detected by monitoring the pose prediction accuracy. Once convergence is reached on the *train set*, latent variables can be estimated on a *test set* of 10k images. With cryoDRGN2, poses from the test set are estimated with a randomly-initialized pose search on the model obtained at train time.

Metrics The error on rotations is given by the median and the mean of the angular error on the view direction, in degrees. The translation error is defined as the median and mean square error of the predicted $\mathbf{t}_i$, in pixels. Before computing pose errors, a rigid 6D-body alignment is applied on the set of predicted poses to align the model into the same global reference frame as the ground truth volume. We perform a Principal Component Analysis (PCA) on the set of predicted z_i's and, looking at the first principal component, we group images in two classes, according to the cluster they fall into. The confusion error is defined as the ratio of misclassified images (images that fall in the wrong

Table 1: Runtime and accuracy for *ab initio* heterogeneous reconstruction on datasets of varying size. Each dataset contains a mix of images, 90% from the *major* volume and 10% from the *minor* volume. After convergence on a train set, each method estimates the latent variables (R_i, $\mathbf{t}_i$, z_i) on a test set. We report the rotation accuracy (Rot. in degrees, ↓), the translation accuracy (Trans. in pixels, ↓), the confusion error (↓) and the resolution (Res. in pixels, ↓). Convergence is detected on the pose accuracy (ep. = epochs).

Dataset / Method	Time	Rot. (Med/MSE)	Trans. (Med/MSE)	Confusion	Res. (major/minor)
Small (Train: 50k / Test: 10k)					
cryoDRGN2 (train)	**1:19h** (20 ep.)	**0.8 / 0.9**	**0.005 / 0.009**	**0**	2.6 / **3.0**
cryoFIRE (train)	1:36h (70 ep.)	2.0 / 2.1	0.06 / 0.09	0.0002	**2.5** / 3.5
cryoDRGN2 (test)	9 min. (3 ep.)	**0.9 / 1.0**	**0.006 / 0.009**	**0**	—
cryoFIRE (test)	**11 sec.** (1 ep.)	1.8 / 1.9	0.18 / 0.27	0.0006	—
Medium (Train: 500k / Test: 10k)					
cryoDRGN2 (train)	5:07h (2 ep.)	**1.1 / 1.1**	**0.006 / 0.009**	0.0002	**2.4 / 2.8**
cryoFIRE (train)	**1:36h** (7 ep.)	2.0 / 2.2	0.08 / 0.11	**0.00008**	2.5 / 3.1
cryoDRGN2 (test)	9 min. (3 ep.)	**1.0 / 1.1**	**0.005 / 0.009**	**0**	—
cryoFIRE (test)	**11 sec.** (1 ep.)	1.7 / 1.9	0.06 / 0.08	**0**	—
Large (Train: 5M / Test: 10k)					
cryoDRGN2 (train)	21:29h (1 ep.)	**1.0 / 1.8**	**0.02** / 1.1	0.0003	**2.2 / 2.5**
cryoFIRE (train)	**1:54h** (1 ep.)	1.5 / 1.7	0.04 / **0.05**	**0.00002**	2.3 / 2.7
cryoDRGN2 (test)	9 min. (3 ep.)	**0.7 / 0.9**	**0.008 / 0.01**	0.009	—
cryoFIRE (test)	**11 sec.** (1 ep.)	1.2 / 1.4	0.03 / 0.04	**0**	—

cluster). After convergence, we generate two volumes by taking the centroids of the clusters in z_i space and conditioning the neural network $\hat{\mathcal{V}}_\theta$ on them. We report the resolution (in pixels) obtained on the major (90%) and on the minor (10%) volumes. The reported resolution is the inverse of the maximum frequency for which the Fourier Shell Correlation is above 0.5.

Results We report the runtime and quantitative metrics in Table 1. At train time, the average time for processing one image is 18 ms (5:07h / ($2 \times 500\,000$)) with cryoDRGN2 vs. 1.7 ms (1:36h / ($7 \times 500\,000$)) for cryoFIRE. (The runtime of cryoDRGN2 is lower with the small dataset because pose search is only done every 5 epochs). At test time, only the encoder of cryoFIRE is used, which further decreases the runtime per image (1.1 ms). The accuracy obtained at test time on ϕ_i and z_i validates that our method effectively amortizes the estimation of latent variables, and the errors on the test sets decrease with the size of the dataset provided for training. The accuracy of predicted poses is slightly worse with cryoFIRE than with an exhaustive pose search strategy (see Supplement E for a comparison with a full non-amortized method [22]). The quantitative resolution of the reconstructed volumes remains however very similar with both methods (see Supplement D for a qualitative comparison).

4.2 Heterogeneous Reconstruction of Synthetic Datasets

Experimental Setup We prepare three heterogeneous datasets of 100k images of the *Plasmodium falciparum* 80S ribosome (Supplement C). The three datasets contain an equal mix of projections from 2, 3 or 10 different ground truth volumes, generated sequentially along a reaction path that corresponds to a rotation of the small ribosomal subunit relative to the large ribosomal subunit identified in [33]. The image formation model is simulated with the same parameters as in Section 4.1. We run cryoFIRE with $d = 8$ and perform a PCA on the set of predicted z_i's after 50 epochs.

Results In Fig. 3, we plot the first principal component (PC1) of the set of z_i's vs. the ground truth index of the volume each image was generated from. With the dataset containing K, images can be clustered in K groups, based on the value of PC1 ($K \in \{2, 3\}$). Looking for the optimal thresholds on PC1, we compute a confusion error of 9×10^{-2} (resp. 5×10^{-3}) on the *2 classes* (resp. *3 classes*) dataset. On the *10 classes* dataset, the 10 conformations cannot be separated but the value of PC1 embeds information about the movement of the ribosome, as indicated by the Spearman correlation [12]. Sampling different values for PC1 (and setting the other components to zero), we can use the neural representation $\hat{\mathcal{V}}_\theta$ to generate a set of volumes from a set of conformational states

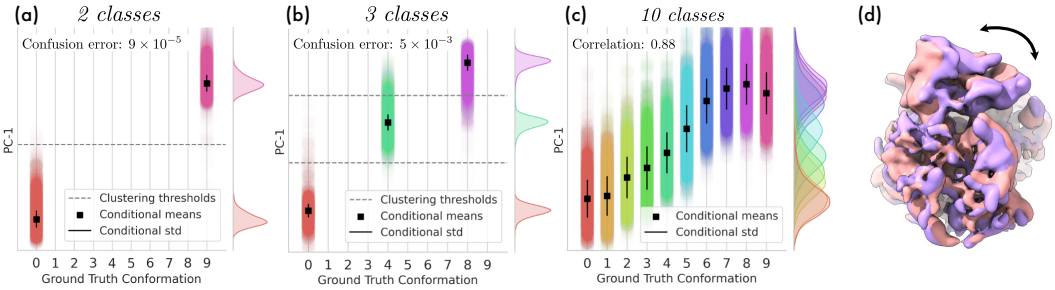

Figure 3: Conformational heterogeneity analysis on synthetic datasets. On (a-b-c), the y-axis shows first principal component (PC1) of a PCA performed on the set of predicted z_i's. We indicate means $\pm$ standard deviations of the PC1s, conditioned on the ground truth conformation. On (a-b) dashed lines are the threshold used to compute the confusion error. Spearman correlation [12] is indicated in (c). (d) is a superposition of two volumes obtained by sampling two points along the PC1 axis for the experiment *2 classes*.

z_i. Qualitative results are given in Fig. 3 (d), showing an accurate reconstruction of the movement of a subunit of the ribosome.

4.3 Heterogeneous Reconstruction of an Experimental Dataset

Experimental Setup We use the publicly available dataset EMPIAR-10180 [19] of a pre-catalytic spliceosome (Supplement C). We run cryoFIRE with $d = 8$, activate the conformation MLP after 30 epochs and train for a total of 100 epochs. Results from cryoDRGN2 [35] and cryoDRGN-BNB [34] on the same dataset are obtained from [35].

Results The first two components of a PCA on the set of predicted z_i's is shown in Fig.4. By traversing the conformational space along the direction of PC1 and generating volumes on set of 5 points, cryoFIRE generates a trajectory, showing a large flexing motion of the spliceosome. CryoFIRE qualitatively recovers the non-uniform distribution of viewing directions, avoids the local minima cryoDRGN-BNB falls into, and reconstructs volumes which qualitatively match the state of the art (Supplement D).

5 Discussion

As the resolving power of a sampling method scales with the size of the dataset, an increasing number of images need to be collected in cryo-EM in order to extract meaningful structural information. CryoFIRE answers the need for reconstruction methods that scale appropriately with the dataset size: heterogeneous *ab initio* reconstruction on a dataset of 5M images can be performed within 2 hours. CryoFIRE is also the first reconstruction method to perform joint amortization of poses and conformations on an experimental cryo-EM dataset, opening the door to fast analysis of structural heterogeneity on real datasets.

CryoFIRE successfully reconstructs heterogeneous distributions. However, the interpretability of the conformational space remains an open question. Since distances in this space are not meaningful (z_i conditions the volume *via* a *nonlinear* decoder), the probability distribution cannot be straightforwardly interpreted in that space. As shown in our experiments, in the case of discrete heterogeneity, general quantities like the number of states or the relative populations of the states can be reliably inferred from the conformational space by clustering the predicted conformational states. In the case of continuous heterogeneity, dimensionality reduction methods like PCA can highlight directions of maximal variance and, by visual inspection of the reconstructed volumes, cryoFIRE can help understanding the main degrees of freedom of a continuously deformable molecule. However, "small" and "large" deformations can stem from similar changes in the conformational space and no physically interpretable notion of distance is currently associated with the conformational space: providing this space with a physically interpretable metric is an interesting avenue for future work, that could lead to exploiting to a larger extent the information embedded in the probability distribution of the conformational states.

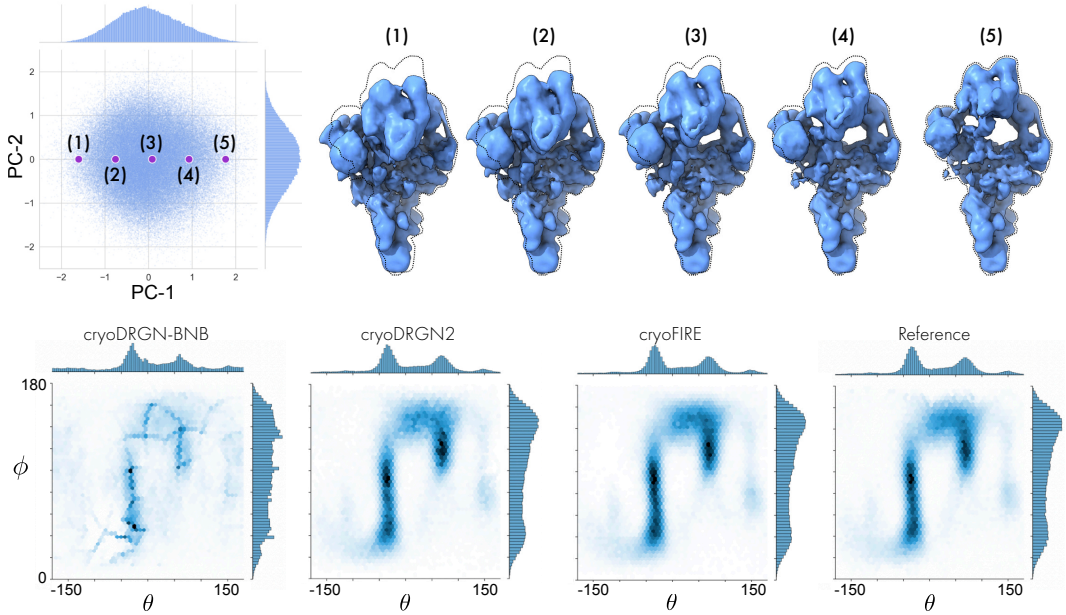

Figure 4: *Ab initio* heterogeneous reconstruction of an experimental dataset of the pre-catalytic spliceosome (EMPIAR-10180 [19]). (Top left) Distribution of the two first principal components of the set of predicted conformational states and sampling points along the first component. (Top right) Structures generated by traversing along PC1. The outline indicates the edges of volume (5). (Bottom) Distribution of the viewing directions in the rotations R_i. The "reference" shows the viewing directions published in [19].

It is worth highlighting that the parameterization proposed here is not uniquely defined: a rotation of the molecule can equivalently be represented by R_i or by a change of conformation state z_i. Empirically, cryoFIRE decorrelates poses and conformation by relying on a "pose-only phase" at the beginning of training and conditioning the pose estimation on the estimated z_i in the encoder, but nothing explicitly prevents z_i from containing information about R_i. Future work could explore improvements in the optimization procedure to further enforce minimal mutual information between poses and conformation.

Finally, we note that the accuracy of pose estimation (especially on translations) is lower with cryoFIRE than with exhaustive pose search methods. Inaccurate translation prediction can lead to "blurry" reconstructions and therefore limits the resolution of reconstructed volumes. This is a direct reflection of the fact that amortization maximizes a non-tight lower-bound of the likelihood, allowing for faster inference at the cost of accuracy [5]. Future work could investigate a hybrid approach that would estimate poses with an encoder at the beginning of training and switch, at the end, to a local pose search initialized from encoder-estimated poses.

Broader Impacts Statement While biomolecular reconstruction from cryo-EM images does not present any obvious ethical challenges, its consequences and its current development as a field calls for careful consideration. The cryo-EM field is generating data at a rapidly increasing pace, potentially leading to wasteful storage and inefficient computing. The design of more efficient methods such as CryoFIRE provides a path to mitigate sustainability risks. In order to better compare modern reconstruction methods, careful attention must be paid toward designing common datasets and evaluation metrics. By providing an open-source implementation of CryoFIRE upon publication, together with benchmark metrics, we hope to make cryo-EM research accessible to a broader class of researchers. We also acknowledge that, by pushing further the boundaries of biological research, our method may facilitate the development of harmful biologics, however this is outweighed by its significant societal benefits, such as enabling antibody-vaccine development [1]. We encourage the cryo-EM community to play wisely with cryoFIRE.

References

[1] Antanasijevic, A., Sewall, L.M., Cottrell, C.A., Carnathan, D.G., Jimenez, L.E., Ngo, J.T., Silverman, J.B., Groschel, B., Georgeson, E., Bhiman, J., et al.: Polyclonal antibody responses to hiv env immunogens resolved using cryoem. Nature communications **12**(1), 1–17 (2021)

[2] Baldwin, P.R., Tan, Y.Z., Eng, E.T., Rice, W.J., Noble, A.J., Negro, C.J., Cianfrocco, M.A., Potter, C.S., Carragher, B.: Big data in cryoem: automated collection, processing and accessibility of em data. Current Opinion in Microbiology **43**, 1–8 (2018)

[3] Bracewell, R.N.: Strip integration in radio astronomy. Australian Journal of Physics **9**, 198–217 (1956)

[4] Chen, M., Ludtke, S.J.: Deep learning-based mixed-dimensional gaussian mixture model for characterizing variability in cryo-em. Nature Methods **18**(8), 930–936 (2021)

[5] Donnat, C., Levy, A., Poitevin, F., Miolane, N.: Deep generative modeling for volume reconstruction in cryo-electron microscop. arXiv preprint arXiv:2201.02867 (2022)

[6] Hartley, R.V.: A more symmetrical fourier analysis applied to transmission problems. Proceedings of the IRE **30**(3), 144–150 (1942)

[7] Herreros, D., Lederman, R.R., Krieger, J., Jiménez-Moreno, A., Martínez, M., Myška, D., Strelak, D., Filipovic, J., Bahar, I., Carazo, J.M., et al.: Approximating deformation fields for the analysis of continuous heterogeneity of biological macromolecules by 3d zernike polynomials. IUCrJ **8**(6) (2021)

[8] Jin, Q., Sorzano, C.O.S., De La Rosa-Trevín, J.M., Bilbao-Castro, J.R., Núñez-Ramírez, R., Llorca, O., Tama, F., Jonić, S.: Iterative elastic 3d-to-2d alignment method using normal modes for studying structural dynamics of large macromolecular complexes. Structure **22**(3), 496–506 (2014)

[9] Kingma, D.P., Ba, J.: Adam: A method for stochastic optimization. arXiv preprint arXiv:1412.6980 (2014)

[10] Kingma, D.P., Welling, M.: Auto-encoding variational bayes. arXiv preprint arXiv:1312.6114 (2013)

[11] Kingma, D.P., Welling, M.: An introduction to variational autoencoders. arXiv preprint arXiv:1906.02691 (2019)

[12] Kokoska, S., Zwillinger, D.: CRC standard probability and statistics tables and formulae. Crc Press (2000)

[13] Lawler, E.L., Wood, D.E.: Branch-and-bound methods: A survey. Operations research **14**(4), 699–719 (1966)

[14] Levy, A., Poitevin, F., Martel, J., Nashed, Y., Peck, A., Miolane, N., Ratner, D., Dunne, M., Wetzstein, G.: Cryoai: Amortized inference of poses for ab initio reconstruction of 3d molecular volumes from real cryo-em images. arXiv preprint arXiv:2203.08138 (2022)

[15] Miolane, N., Poitevin, F., Li, Y.T., Holmes, S.: Estimation of orientation and camera parameters from cryo-electron microscopy images with variational autoencoders and generative adversarial networks. In: Proceedings of the IEEE/CVF Conference on Computer Vision and Pattern Recognition Workshops. pp. 970–971 (2020)

[16] Nakane, T., Kimanius, D., Lindahl, E., Scheres, S.H.: Characterisation of molecular motions in cryo-em single-particle data by multi-body refinement in relion. elife **7**, e36861 (2018)

[17] Namba, K., Makino, F.: Recent progress and future perspective of electron cryomicroscopy for structural life sciences. Microscopy **71**, i3–i14 (2022)

[18] Nashed, Y.S., Poitevin, F., Gupta, H., Woollard, G., Kagan, M., Yoon, C.H., Ratner, D.: Cryoposenet: End-to-end simultaneous learning of single-particle orientation and 3d map reconstruction from cryo-electron microscopy data. In: Proceedings of the IEEE/CVF International Conference on Computer Vision. pp. 4066–4076 (2021)

[19] Plaschka, C., Lin, P.C., Nagai, K.: Structure of a pre-catalytic spliceosome. Nature **546**(7660), 617–621 (2017)

[20] Punjani, A., Fleet, D.J.: 3d flexible refinement: structure and motion of flexible proteins from cryo-em. BioRxiv (2021)

[21] Punjani, A., Fleet, D.J.: 3d variability analysis: Resolving continuous flexibility and discrete heterogeneity from single particle cryo-em. Journal of Structural Biology **213**(2), 107702 (2021)

[22] Punjani, A., Rubinstein, J.L., Fleet, D.J., Brubaker, M.A.: cryosparc: algorithms for rapid unsupervised cryo-em structure determination. Nature methods **14**(3), 290–296 (2017)

[23] Rohou, A., Grigorieff, N.: Ctffind4: Fast and accurate defocus estimation from electron micrographs. Journal of structural biology **192**, 216–221 (2015)

[24] Rosenbaum, D., Garnelo, M., Zielinski, M., Beattie, C., Clancy, E., Huber, A., Kohli, P., Senior, A.W., Jumper, J., Doersch, C., et al.: Inferring a continuous distribution of atom coordinates from cryo-em images using vaes. arXiv preprint arXiv:2106.14108 (2021)

[25] Rosenthal, P.B., Henderson, R.: Optimal determination of particle orientation, absolute hand, and contrast loss in single-particle electron cryomicroscopy. Journal of molecular biology **333**, 721–745 (2003)

[26] Scheres, S.H.: RELION: Implementation of a Bayesian approach to cryo-EM structure determination. Journal of Structural Biology **180**, 519–530 (2012)

[27] Scheres, S.H., Gao, H., Valle, M., Herman, G.T., Eggermont, P.P., Frank, J., Carazo, J.M.: Disentangling conformational states of macromolecules in 3d-em through likelihood optimization. In: Single-Particle Cryo-Electron Microscopy: The Path Toward Atomic Resolution: Selected Papers of Joachim Frank with Commentaries, pp. 413–415. World Scientific (2018)

[28] Simonyan, K., Zisserman, A.: Very deep convolutional networks for large-scale image recognition. arXiv preprint arXiv:1409.1556 (2014)

[29] Singer, A., Sigworth, F.J.: Computational methods for single-particle electron cryomicroscopy. Annual Review of Biomedical Data Science **3**, 163–190 (2020)

[30] Tagare, H.D., Kucukelbir, A., Sigworth, F.J., Wang, H., Rao, M.: Directly reconstructing principal components of heterogeneous particles from cryo-em images. Journal of structural biology **191**(2), 245–262 (2015)

[31] Tancik, M., Srinivasan, P., Mildenhall, B., Fridovich-Keil, S., Raghavan, N., Singhal, U., Ramamoorthi, R., Barron, J., Ng, R.: Fourier features let networks learn high frequency functions in low dimensional domains. Advances in Neural Information Processing Systems **33**, 7537–7547 (2020)

[32] Vulović, M., Ravelli, R.B.G., van Vliet, L.J., Koster, A.J., Lazić, I., Lücken, U., Rullgård, H., Öktem, O., Rieger, B.: Image formation modeling in cryo-electron microscopy. Journal of Structural Biology **183**, 19–32 (2013)

[33] Zhong, E.D., Bepler, T., Berger, B., Davis, J.H.: Cryodrgn: reconstruction of heterogeneous cryo-em structures using neural networks. Nature methods **18**(2), 176–185 (2021)

[34] Zhong, E.D., Bepler, T., Davis, J.H., Berger, B.: Reconstructing continuous distributions of 3d protein structure from cryo-em images. arXiv preprint arXiv:1909.05215 (2019)

[35] Zhong, E.D., Lerer, A., Davis, J.H., Berger, B.: Cryodrgn2: Ab initio neural reconstruction of 3d protein structures from real cryo-em images. In: Proceedings of the IEEE/CVF International Conference on Computer Vision. pp. 4066–4075 (2021)

[36] Zhong, E.D., Lerer, A., Davis, J.H., Berger, B.: Exploring generative atomic models in cryo-em reconstruction. arXiv preprint arXiv:2107.01331 (2021)

[37] Zhou, Y., Barnes, C., Lu, J., Yang, J., Li, H.: On the Continuity of Rotation Representations in Neural Networks. arXiv: 1812.07035 (2020)

Checklist

1. For all authors...
   (a) Do the main claims made in the abstract and introduction accurately reflect the paper's contributions and scope? [Yes]
   (b) Did you describe the limitations of your work? [Yes] see Sec. 5
   (c) Did you discuss any potential negative societal impacts of your work? [N/A]
   (d) Have you read the ethics review guidelines and ensured that your paper conforms to them? [Yes]
2. If you are including theoretical results...
   (a) Did you state the full set of assumptions of all theoretical results? [N/A]
   (b) Did you include complete proofs of all theoretical results? [N/A]
3. If you ran experiments...
   (a) Did you include the code, data, and instructions needed to reproduce the main experimental results (either in the supplemental material or as a URL)? [No] We plan on making code available.
   (b) Did you specify all the training details (e.g., data splits, hyperparameters, how they were chosen)? [Yes]
   (c) Did you report error bars (e.g., with respect to the random seed after running experiments multiple times)? [No]
   (d) Did you include the total amount of compute and the type of resources used (e.g., type of GPUs, internal cluster, or cloud provider)? [Yes] see Sec. 4
4. If you are using existing assets (e.g., code, data, models) or curating/releasing new assets...
   (a) If your work uses existing assets, did you cite the creators? [Yes]
   (b) Did you mention the license of the assets? [No]
   (c) Did you include any new assets either in the supplemental material or as a URL? [No]
   (d) Did you discuss whether and how consent was obtained from people whose data you're using/curating? [N/A]
   (e) Did you discuss whether the data you are using/curating contains personally identifiable information or offensive content? [No]
5. If you used crowdsourcing or conducted research with human subjects...
   (a) Did you include the full text of instructions given to participants and screenshots, if applicable? [N/A]
   (b) Did you describe any potential participant risks, with links to Institutional Review Board (IRB) approvals, if applicable? [N/A]
   (c) Did you include the estimated hourly wage paid to participants and the total amount spent on participant compensation? [N/A]